Dalton Transactions

ROYAL SOCIETY OF CHEMISTRY

PAPER

View Article Online
View Journal | View Issue

Check for updates

Cite this: *Dalton Trans.*, 2024, **53**, 9062

New cyanido-bridged iron(II) spin crossover coordination polymers with an unusual ladder-like topology: an alternative to Hofmann clathrates†

Diana Visinescu, [a] Sergii I. Shylin, [b] Sergiu Shova,[c] Ghenadie Novitchi,*[d] Delia-Laura Popescu[e] and Maria-Gabriela Alexandru *[f]

Received 24th March 2024,
Accepted 29th April 2024

DOI: 10.1039/d4dt00870g

rsc.li/dalton

Two new cyanido-bridged {$Fe^{II}M^{II}$} double chains were obtained by reacting cyanido anions $[M(CN)_4]^{2-}$ with complex cations $[Fe^{II}(tptz)]^{2+}$ (preformed *in situ* by mixing a hydrated tetrafluoroborate salt of iron(II) and a tptz ligand, tptz = 2,4,6-tri(2-pyridyl)-1,3,5-triazine) having the general formula $[Fe^{II}(tptz)M^{II}(CN)_4]\cdot 2H_2O\cdot CH_3CN$, where M = Pd (**1**) or Pt (**2**). Additionally, two molecular complexes formulated as $[Fe^{II}(tptz)_2][M^{II}(CN)_4]\cdot 4.25H_2O$, where M = Pd (**3**) or Pt (**4**), were subsequently obtained from the same reaction, as secondary products. Single crystal X-ray analysis revealed that **1** and **2** are isostructural and crystallize in the *P*-1 triclinic space group. Their structure consists of a double-chain with a ladder-like topology, in which cyanido-based $[M(CN)_4]^{2-}$ metalloligands coordinate, through three CN^- ligands and three $[Fe^{II}(tptz)]^{2+}$ complex cations. Compounds **3** and **4** are also isostructural and crystallize in the $P\bar{1}$ triclinic space group, and the X-ray structural data show the formation of $[Fe^{II}(tptz)_2]^{2+}$ and $[M^{II}(CN)_4]^{2-}$ ionic units interconnected through H-bonds and π···π stacking supramolecular interactions. The static DC magnetic measurements recorded in the temperature range of 2–300 K showed that **1** and **2** exhibit incomplete spin transition on cooling, which is also confirmed by single crystal XRD analysis and Mössbauer spectroscopy. Compounds **3** and **4** are diamagnetic, most likely due to the encapsulation of Fe(II) in a tight pocket formed by two tptz ligands that preserve the low-spin state in the temperature range of 2–400 K.

Introduction

Coordination compounds exhibiting spin crossover (SCO) behavior are of high interest for their applications in information storage devices, microthermometry, as well as molecular switches, thermochromic materials, sensors and actuators; therefore several critical reviews have been devoted to this subject.[1–12] The SCO phenomenon is found in a certain series of $3d^4$–$3d^7$ metal complexes, but most of the examples are mononuclear coordination compounds of Fe(II) with the $3d^6$ configuration. Polydentate ligands such as pyrazole-pyridine/pyrazine or imidazole derivatives were extensively employed to create the N_6 environment around Fe(II) ions, which proved to be favorable towards a spin switching behavior.[1,2,4,12] Several iron(II)-bearing SCO complexes with six-N_4O_2,[13] N_5O,[14] N_5Cl,[15] N_4S_2,[16] N_5S,[17] and N_4C_2,[18] seven-$N_3C_2O_2$[19] or four-C_3N[20] coordination surrounding have also been reported. In the case of thermally induced SCO, cooperativity is the key in defining the shape of the transition, *i.e.* its abruptness and eventual thermal hysteresis. The cooperative effect between the SCO centers can be enhanced by using suitable bridging (metallo) ligands to connect the ferrous ions into chains or high-dimen-

[a]*Coordination and Supramolecular Chemistry Laboratory, "Ilie Murgulescu" Institute of Physical Chemistry, Romanian Academy, Splaiul Independentei 202, Bucharest 060021, Romania*
[b]*Department of Chemistry – Ångström Laboratory, Uppsala University, 75120 Uppsala, Sweden*
[c]*Petru Poni Institute of Macromolecular Chemistry, Romanian Academy, Aleea Grigore Ghica Vodă 41-A, RO-700487 Iasi, Romania*
[d]*Laboratoire National des Champs Magnétiques Intenses (LNCMI), Univ. Grenoble Alpes, EMFL, CNRS 38042 Grenoble, France. E-mail: ghenadie.novitchi@lncmi.cnrs.fr*
[e]*Faculty of Chemistry, University of Bucharest, Regina Elisabeta Blvd 4-12, Bucharest 030018, Romania*
[f]*Department of Inorganic Chemistry, Physical Chemistry and Electrochemistry, Faculty of Chemical Engineering and Biotechnologies, National University of Science and Technology Politehnica of Bucharest, 1-7 Gh. Polizu Street, 011061 Bucharest, Romania. E-mail: maria.alexandru@up.ro*

†Electronic supplementary information (ESI) available: FTIR spectra (Figs. S1–S4, **1**–**4**); UV-Vis spectra (Figs. S5 and S6, **1**–**4**), PXRD patterns (Figs. S7–S9, **1**–**4**); asymmetric unit and fragment of the double chain of **2** (Fig. S11); packing diagram of **1** and **2** (Figs. S10, S12 and S13); and drawing of the packing diagrams of **3** and **4**, structure of **4** (Figs. S14–S16); χT *vs.* *T* curve for **1** fitted with the Slichter–Drickamer model (Fig. S17); crystallographic data (Tables S1 and S2, **1**–**4**), SHAPE analysis (Table S3, **1**–**4**) and H-bond parameters (Tables S4–S7, **1**–**4**). CCDC 2342169–2342173. For ESI and crystallographic data in CIF or other electronic format see DOI: https://doi.org/10.1039/d4dt00870g

sional networks, and also through supramolecular interactions such as hydrogen bonds and/or π···π stacking, or guest molecules within the lattice.[12,21–24]

The node and spacer strategy proved to be efficient in the assembly of Fe(II)-bearing SCO coordination polymers exhibiting rich and fascinating structural features and magnetic behavior. Hofmann type structures represent the largest class of SCO 2-D or 3-D coordination polymers.[10] The structure of Hofmann clathrate analogues usually consists of planar or corrugated cyanido-bridged $[Fe^{II}M_x(CN)_y]^{n-}$ heterometallic layers pillared by monodentate N-donor heterocyclic ligands coordinated to Fe(II), disposed in a *trans* arrangement. Among the examples, $[M^{I}(CN)_2]^-$ (M^{I} = Au and Ag) dicyanidometallates were efficient platforms for constructing extended networks exhibiting a wide range of spin transitions.[25–28] Also suitable for constructing Hofmann type SCO networks are cyanido-based (metallo)ligands of late transition metals, for example $[M^{II}(CN)_4]^{2-}$ (M^{II} = Ni, Pd, and Pt).[29–33] A compelling study was carried out on 3-D Hofmann-like clathrate metal–organic frameworks of the formula $\{Fe(bpac)[M(CN)_4]\}\cdot H_2O\cdot x(bpac)$ (M = Pt, Pd, and Ni; bpac = bis(4-pyridyl)acetylene), for which the SCO with a pronounced hysteresis occurred and was a result of the interactions between the SCO centers mediated by bpac guest molecules.[29] Another porous 3-D coordination polymer, $[Fe(dpsme)Pt(CN)_4]\cdot 2/3dpsme\cdot x EtOH\cdot yH_2O$ (dpsme = 4,4′-di(pyridylthio)methane; EtOH = ethanol), which exhibits a three-step SCO with hysteresis, was reported by Kepert *et al.*[30]

Regarding other structural types, fewer SCO compounds based on $[M^{IV/V}(CN)_8]^{4-/3-}$ (M = Re, Nb, Mo, and W) were also reported, with 3-D $\{Fe^{II}_2(3\text{-}OAcpy)_5(3\text{-}OHpy)_3[M^{IV}(CN)_8]\}\cdot nH_2O$ (M = Mo, n = 0, FeMo; M = Nb, n = 1, FeNb),[34] and 2D $Cs\{[Fe(3\text{-}CNpy)_2][Re(CN)_8]\}\cdot H_2O$ frameworks being the most notable examples showing thermally induced spin transition (3-OAcpy = 3-acetoxypyridine; 3-OHpy = 3-hydroxypyridine; 3-CNpy = 3-cyanopyridine).[35] Also, an interesting example is represented by the chiral SCO 3-D cyanido-bridged bimetallic compound, of the formula $Fe^{II}_2[Nb^{IV}(CN)_8](4\text{-bromopyridine})_8\cdot 2H_2O$, assembled from the Nb(IV) diamagnetic metalloligand connecting Fe(II) nodes, which underwent an incomplete SCO process.[36]

The exploration of pincer ligands is very attractive for constructing Fe(II)-containing coordination polymers with different dimensionalities and architectures. In this regard, the polydentate planar, rigid, and bulky tptz molecule (tptz = 2,4,6-tri(2-pyridyl)-1,3,5-triazine) is an N-donor ligand featuring three 2-pyridyl rings and one 1,3,5-triazine ring with multiple chelating coordination sites. The tptz molecule was extensively exploited as a ligand for lanthanide or transition metal ions due to its various coordinating modes acting as a mono- or bis-tridentate or/and bidentate ligand.[37–41] These d/f frameworks, with different topologies, showed interesting magnetic, chiral and luminescence properties.[37–41] Moreover, complex cations with tptz and $\{M(tptz)\}^{n+}$ were also used as building blocks to assemble, in combination with cyanido-based metalloligands, cyanido-bridged d–d′ or d–f heterometallic complexes, such as $[Mn^{II}(tptz)(H_2O)(NO_3)(\mu\text{-}NC)Cr^{III}(ampy)(CN)_3]\cdot CH_3CN$ and $[Mn^{II}(tptz)(H_2O)(NO_3)(\mu\text{-}NC)Cr^{III}(phen)(CN)_3]\cdot H_2O$ binuclear complexes (ampy = 2-aminomethylpyridine and phen = 1,10-phenanthroline),[42] and $\{Fe^{III}_4M^{II}_2\}$ hexanuclear (M = Fe, Co, and Ni)[43] or $\{Fe^{III}Ln^{III}\}$ chains (Ln = Pr, Nd, Sm, Eu, and Gd).[44]

The reports of iron(III)[45] and iron(II)[43,44,46] complexes meridionally capped with triazine-derived pincer ligands are very scarce. Thus, the mononuclear iron(II)-bearing complex with the tptz ligand, $[Fe^{II}(tptzH)_2](ClO_4)_4$, is diamagnetic in the range of 2–300 K.[46] Another example, the cyanido-bridged $\{Fe^{III}_4Fe^{II}_2\}$ heterometallic complex assembled from $[Fe^{II}(tptz)]^{2+}$ and $[Fe^{III}(Tp^*)(CN)_3]^-$ moieties (Tp* = tris(3,5-dimethylpyrazol-1-yl)borohydride) exhibited intervalence charge transfer between Fe(II) and Fe(III) ions.[43] To our knowledge, there is no report of complexes containing the $\{Fe^{II}(tptz)\}$ moiety that show spin transition. Herein, we report the synthesis and magneto-structural characterization of two new cyanido-bridged $\{[Fe^{II}(tptz)(\mu\text{-}CN)_3M^{II}(CN)]\cdot 2H_2O\cdot CH_3CN\}_n$ double chains exhibiting incomplete SCO (M = Pd (**1**) and Pt (**2**)), and two diamagnetic salts of complex cation-complex anion type, $[Fe^{II}(tptz)_2][M^{II}(CN)_4]\cdot 4.25H_2O$, in which the low-spin state of the Fe(II) metal ion is preserved in the temperature range of 2–400 K, where M = Pd (**3**) and Pt (**4**).

Experimental

The chemicals used were of reagent grade and were purchased from commercial sources.

Synthesis

0.031 g of tptz (0.1 mmol) was dissolved in 5 mL of acetonitrile and was mixed with a solution of 0.034 g of $Fe(BF_4)_2\cdot 6H_2O$ (0.1 mmol) in 5 mL of acetonitrile. The obtained violet solution was layered upon a solution of 0.037 g of $K_2[Pd(CN)_4]$ (**1**)/0.030 g $K_2[Pd(CN)_4]$ (**2**) (0.1 mmol) dissolved in 5 mL of distilled water. Small violet rod-like crystals of **1** and **2**, respectively, were formed in two weeks. The crystals were collected, and the solution was further left standing and, after five days, compounds **3** and **4**, respectively, crystallized as large violet blocks. Yield: *ca.* 30% based on tptz (**1**). Anal. Calcd for $C_{24}H_{19}N_{11}O_2FePd$ (**1**): C, 43.96; H, 2.92; N, 23.49. Found: C, 43.87; H, 3.02; N, 23.43%. IR (KBr/cm^{-1}): 3429s, 2159vs and 2136w [ν_{CN}, cyanide] and 1606vs, 1557s, [$\nu_{C=N}$], 1532s, 1380s, 1364s, 998s, 496m and 415m. Yield: *ca.* 35% based on tptz (**2**). Anal. Calcd for $C_{24}H_{19}N_{11}O_2FePt$ (**2**): C, 38.72; H, 2.57; N, 20.69. Found: C, 38.69; H, 2.52; N, 20.71%. IR (KBr/cm^{-1}): 3388s, 2162s, and 2135s [ν_{CN}, cyanide], 1608vs, 1566, and 1532s [$\nu_{C=N}$], 1010s, 889s, 495m and 411m. Yield: *ca.* 35% based on tptz (**3**). Anal. Calcd for $C_{24}H_{19}N_{11}O_2FePd$ (**3**): C, 43.96; H, 2.92; N, 23.49. Found: C, 43.87; H, 3.02; N, 23.43%. IR (KBr/cm^{-1}): 3438s, 2250w, 2131s [ν_{CN}, cyanide] and 1619vs, 1471s, 1305s, 459m and 437m [$\nu_{C=N}$]. Yield: *ca.* 35% based on tptz (**4**). Anal. Calcd for $C_{24}H_{19}N_{11}O_2FePt$ (**4**): C, 38.72; H, 2.57; N, 20.69. Found: C, 38.69; H, 2.52; N, 20.71%. IR (KBr/cm^{-1}):

3438s, 2250w, 2128s [ν_{CN}, cyanide], and 1619vs, 1471s, 1305s, 459m and 437m [$\nu_{C=N}$].

Physical measurements

Elemental analyses (C, H, N) were performed with a PerkinElmer 2400 analyzer. The IR spectra of **1–4** were recorded on a FTIR Bruker Tensor V-37 spectrophotometer as KBr pellets in the 4000–400 cm^{-1} range, at room temperature. UV-Vis spectra (diffuse reflectance technique) for **1–4** were recorded on a 200–1000 nm domain with a JASCO V-670 spectrophotometer, using MgO as a standard. X-ray powder diffraction data were recorded on a Proto AXRD benchtop using Cu Kα radiation with a wavelength of 1.54059 Å in the range of 5–35° (2θ).

X-ray data collection and structure refinement

Single-crystal X-ray diffraction data were collected on an Oxford-Diffraction XCALIBUR Eos CCD diffractometer with graphite-monochromated Mo Kα. Unit cell determination and data integration were carried out using the CrysAlisPro package from Oxford Diffraction.[47] Multi-scan correction for absorption was applied. The structures were solved with the ShelXT program using the intrinsic phasing method and refined by the full-matrix least-squares method on F^2 with ShelXL.[48,49] Olex2 was used as an interface to the ShelX programs.[50] The drawing of the molecules was performed using the Diamond 4 program.[51] Non-hydrogen atoms were refined anisotropically. Hydrogen atoms were placed geometrically and refined using a riding model. The assignment of the C and N atoms in the cyanide group was done using a disorder model involving a shared occupation of 50 : 50 for C and N atoms. Detailed crystallographic data for **1** (at 180 and at 100 K), **2**, **3** and **4** are provided in Table 1. Selected bond lengths and angles for **1** (at 180 and at 100 K), **2**, **3** and **4** are gathered in Tables S1 and S2 in the ESI.† Specific details of each refinement are given in the crystallographic information files (CIF-files). CCDC numbers: 2342169 (**1** at 180 K), 2342170 (**1** at 101 K), 2342171 (**2**), 2342172 (**3**) and 2342173 (**4**).†

Magnetic properties

DC magnetic susceptibility data (2–300 K) were collected on powdered samples using a SQUID magnetometer (Quantum Design MPMS-XL), applying a magnetic field of 0.1 T. All data were corrected for the contribution of the sample holder and the diamagnetism of the samples estimated from Pascal's constants.[52,53] The field dependence of the magnetization (up to 5 T) was measured between 2.0 and 5.0 K. Data analysis was performed using MATLAB involving EasySpin software.[54] Minimization was performed using the *fmincon* function with the Interior-Point Algorithm.

^{57}Fe Mössbauer spectroscopy

^{57}Fe Mössbauer spectra were recorded using a constant-acceleration spectrometer (Wissel), equipped with a nitrogen flow cryostat, with a ^{57}Co source embedded in a rhodium matrix. Absorbers were prepared by placing the powdered samples in poly(methyl methacrylate) holders. Fitting of the experimental data was performed with Recoil software. Hyperfine parameters uncertainties were evaluated from the covariance matrix of the fit. Isomer shifts are presented relative to the iron metal at ambient temperature.

Results and discussion

The reaction of $[M(CN)_4]^{2-}$ metalloligands with $[Fe^{II}(tptz)]^{2+}$ complex cations, formed *in situ* by mixing ferrous tetrafluoroborate with tptz, afforded two structural types, the cyanido-

Table 1 Crystal data and details of structure refinement for **1–4**

Compound	**1** (180 K)	**1** (101 K)	**2**	**3**	**4**
Emp. formula	$C_{24}H_{19}FeN_{11}O_2Pd$	$C_{24}H_{19}FeN_{11}O_2Pd$	$C_{24}H_{19}FeN_{11}O_2Pt$	$C_{40}H_{31.34}FeN_{16}O_{3.17}Pd$	$C_{40}H_{31}FeN_{16}O_{3.5}Pt$
F_w	655.75	655.75	744.44	949.03	1042.75
T [K]	180	100	120	293	101
Space group	$P\bar{1}$	$P\bar{1}$	$P\bar{1}$	$P\bar{1}$	$P\bar{1}$
a [Å]	9.2277(6)	9.1702(6)	9.2213(8)	9.8400(8)	9.75831(17)
b [Å]	10.5250(6)	10.3930(6)	10.5204(7)	11.7209(9)	11.66423(18)
c [Å]	15.0648(6)	15.0356(10)	15.0384(13)	18.2393(15)	18.0933(3)
α [°]	94.888(4)	94.756(5)	95.003(3)	101.995(7)	102.3695(13)
β [°]	93.429(4)	94.062(5)	93.519(2)	93.012(7)	92.7038(14)
γ [°]	116.505(6)	115.990(6)	116.499(14)	102.090(6)	102.3721(14)
V [Å^3]	1296.70(14)	1274.41(15)	1292.4(2)	2001.9(3)	1955.54(6)
Z	2	2	2	2	2
ρ_{calcd} [g cm^{-3}]	1.679	1.709	1.913	1.574	1.771
μ [mm^{-1}]	1.298	1.321	6.013	0.874	4.009
Crystal size [mm]	0.06 × 0.03 × 0.01	0.25 × 0.10 × 0.03	0.04 × 0.02 × 0.02	0.15 × 0.15 × 0.03	0.07 × 0.05 × 0.03
2Θ range	4.358 to 58.368	4.874 to 50.046	4.362 to 50.046	3.646 to 58.632	4.676 to 52.744
Refls. collected	11 197	7027	46 290	10 550	27 657
Indep. Refls., R_{int}	5891, 0.0283	7027, 0.0217	4557, 0.0262	10 550, 0.054	7948, 0.0393
Data/rests./params.	5891/15/365	7027/28/360	4557/4/356	10 550/20/582	7948/54/570
GOF	1.040	1.061	1.030	1.077	1.011
R_1, wR_2(all data)	0.0386, 0.0712	0.0419, 0.1226	0.0131, 0.0316	0.0314, 0.0839	0.0509, 0.1663
CCDC no.	2342169	2342170	2342171	2342172	2342173

bridged $\{Fe^{II}M^{II}\}$ double chains M = Pd (**1**) and M = Pt (**2**), respectively, and, subsequently, the complex cation-complex anion molecular compounds, namely $[Fe^{II}(tptz)_2][M^{II}(CN)_4]$, M = Pd (**3**) and M = Pt (**4**), respectively. The single crystals of **1** and **2** grew as small prisms and were separated by filtration, whereas **3** and **4**, which are much more soluble in the solvent mixture, crystallized as large cubes from the filtrate solution of **1** and **2**, after several days. The FTIR spectra show two bands, at 2162 and 2136 cm^{-1} for **1**, and 2159 and 2136 cm^{-1} for **2**, which are characteristic for the stretching vibrations of the cyanido bridging and terminal ligands, Fig. S1 and S2 in the ESI.† For the ionic salts, **3** and **4**, the bands at 2131 and 2129 cm^{-1}, respectively, confirm the existence of terminal cyanido ligands, only, Fig. S3 and S4 in the ESI† (similar wavenumbers as in the case of the terminal cyanido ligands in **1** and **2**). The strong bands at 1606 and 1557 cm^{-1} for **1**, and those at 1608 and 1578 cm^{-1} for **2**, can be assigned to the stretching vibrations of the aromatic C═N and C═C bonds belonging to the tptz ligand. The aromatic ring vibrations appear as bands at 1380, 998, and 769 cm^{-1} for **1**, and 1378, 1010, and 768 cm^{-1} for **2**. Similar bands assigned to the tptz vibrations appeared for **3** and **4**. The UV–Vis spectrum shows a broad, high intensity band at 570 and 580 nm for **1** and **2**, respectively, assigned to the metal-to-ligand charge-transfer (MLCT) transition coming from the $[Fe(tptz)_2]^{2+}$ unit, as shown in Fig. S5 in the ESI.†[55,56] Broad bands at *ca.* 690, 570 and 515 nm are shown for **3** and **4**, most likely arising from the MLCT process (Fig. S6 in the ESI†). In both cases, the bands appearing up to 400 nm can be ascribed to the π–π transitions within the tptz ligand. The powder XRD data of **1–4** are very similar to the calculated ones from the single-crystal X-ray diffraction data, as shown in Figs. S7–S9 in the ESI.†

Crystal structure description

Compounds **1** and **2** are isostructural and, therefore, we will describe only the structure of **1**. Compound **1** crystallizes in the triclinic system, with the space group $P\bar{1}$ and its structure consists of neutral double-chains of edge-sharing squares and ladder-like topology, with formula: $\{[Fe^{II}(tptz)(\mu\text{-}NC)_3Pd^{II}(tptz)(CN)]\cdot 2H_2O\cdot CH_3CN\}_n$ that grow along the *b* crystallographic axis. The asymmetric unit, shown in Fig. 1, left, consists of a cyanido-bridged $\{Fe^{II}Pd^{II}\}$ dinuclear moiety assembled from a $[Pd^{II}(CN)_4]^{2-}$ metalloligand which coordinates through one cyanido group, C19N7, to one $[Fe^{II}(tptz)]^{2+}$ unit (for compound **2**, see Fig. S10 in the ESI†). Each bimetallic unit further coordinates, through two cyanide ligands, in a *cis* manner, and two neighboring $\{Fe^{II}Pd^{II}\}$ moieties assembling a double-chain with a 1-D ladder topology along an axis parallel to the *b* crystallographic axis, shown in Fig. 1, right. Each Fe^{II} ion has an N_6 coordination environment, being surrounded by three N atoms from cyanido bridging ligands and three N donor atoms belonging to the tptz molecule, in a distorted octahedral geometry [the estimated ChSM value is 2.653 for Fe1, being zero for the ideal octahedron as predicted by the SHAPE program;[57,58] see Table S3 in the ESI† **1**]. The values of the $Fe1\text{–}N_{cyanide}$ bond lengths range between 2.090(3) for Fe1–N7 and 2.180(3) Å for Fe1–N9a, while the $Fe1\text{–}N_{tptz}$ bond distances are longer [Fe1–N1 = 2.249(3), Fe1–N2 = 2.129(2), and 2.246(3) Å, symmetry code: (a) = $-x$, $1-y$, $1-z$] due to a higher affinity of Fe^{II} for negatively charged cyanometallates than for the neutral tptz molecule.[32] These values, obtained when the crystals were measured at 180 K, correspond to a high-spin state of the Fe(II) ion. The Fe–N bond length decreases when the measurements were performed at 101 K, as shown in Table 2, with the largest difference of 0.087 and the smallest, 0.043 Å. This indicates that Fe(II) undergoes an SCO process, from a high-spin state to a low-spin state.

The Pd(II) ion is coordinated by four cyanido ligands in a square planar geometry with almost right angles between the neighboring cyanide groups: 90.91(11) [for C20–Pd1–C22] and 87.91(11)° [for C22–Pd1–C21]. The Pd–C bond lengths vary between 1.990(3) and 1.994(3) Å (for Pd1–C22 and Pd1–C21,

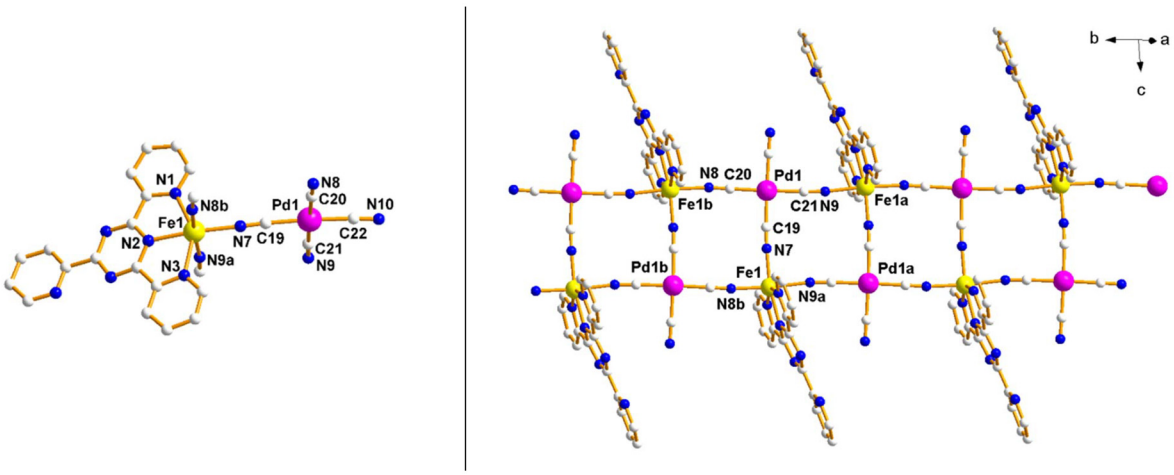

Fig. 1 Left: asymmetric unit of **1**, together with the atom labelling scheme. Right: fragment of the ladder-like double chain **1**. Symmetry codes: (a) = $-x$, $1-y$, $1-z$; (b) = $-x$, $2-y$, $1-z$.

Table 2 Bond distances involving the Fe(II) atom in **1**

Fe–N bonds	Length/Å at 180 K	Length/Å at 101 K
Fe1–N1	2.249(3)	2.186(5)
Fe1–N2	2.129(2)	2.042(5)
Fe1–N3	2.246(3)	2.163(5)
Fe1–N7	2.090(3)	2.047(5)
Fe1–N8b[a]	2.180(3)	2.099(5)
Fe1–N9a[a]	2.111(3)	2.046(5)

[a] Symmetry codes: (a) = $-x$, $1-y$, $1-z$; (b) = $-x$, $2-y$, $1-z$.

respectively). The cyanido metalloligand coordinates to the Fe(II) atom at angles close to linearity, ranging between 175.9(3) (Fe1–N7–C19) and 173.7(2)° (Fe1a–N8–C20, symmetry code (a) = $-x$, $1-y$, $1-z$).

The analysis of the packing diagram indicates the formation of a 3-D supramolecular network with cyanido-bridged $\{Fe^{II}Pd^{II}\}$ ladder-like double chains connected through hydrogen bonds involving $N_{cyanido}$ and $N_{pyridine}$ atoms and solvent water molecules as shown in Fig. 2, left, Fig. S11 and Table S4 in the ESI (and Fig. S12 and Table S5 in the ESI† for **2**), and $\pi\cdots\pi$ stacking interactions between the aromatic rings, as shown in Fig. 2, right.

Four-atom supramolecular rings were formed from solvent water molecules (O1W···O2W···O1Wy···O2Wy) connected through H-bonds which can be described as the $R^2_2(4)$ graph set, with symmetry code (y) = $-x$, $2-y$, $2-z$. The small water clusters "bridge" the neighboring chains, the water molecules acting also as H-donors for peripheral tptz and cyanide ligands [N_{tptz} (N6) and $N_{cyanido}$ (N10) acceptor atoms] building in this manner a 3-D supramolecular network, as shown in Fig. S10 in the ESI.† The face-to-face $\pi\cdots\pi$ stacking interactions shown in Fig. 2, left, are characterized by the centroid–centroid distance of *ca.* 3.66 Å (for compound **2**, see Fig. S13 in the ESI†).

Compounds **3** and **4** are also isostructural and crystallize in the triclinic system, with the space group $P\bar{1}$. Since they are isostructural, we will describe only compound **3**. Its structure is made up from complex ions, the charge of the $[Fe(tptz)_2]^{2+}$ cation being balanced by halves of two $[Pd(CN)_4]^{2-}$ anions, as shown in Fig. 3, left (for compound **4**, see Fig. S14, left, in the ESI†). Unlike **1** and **2**, the eight coordination environment of iron(II) is saturated with two meridionally coordinated tptz

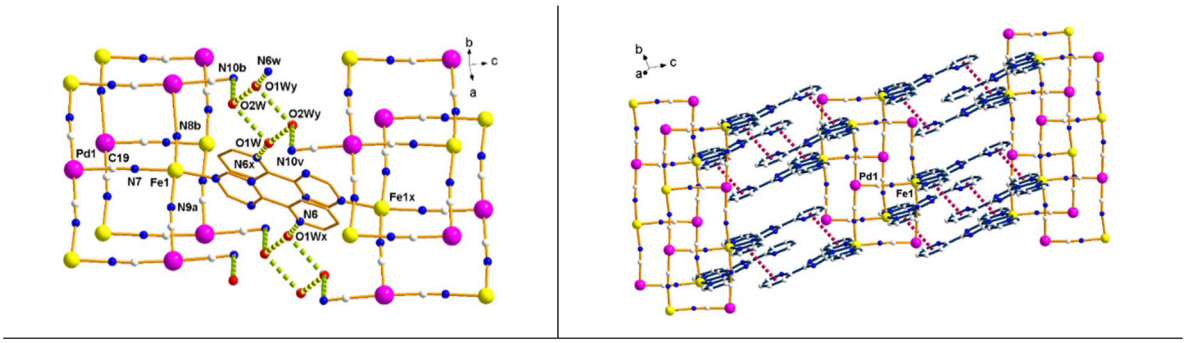

Fig. 2 Details of crystal packing in **1** showing: left, the H-bonds (green dotted lines) established in **1** [(b) = $-x$, $2-y$, $1-z$; (v) = x, y, $1+z$; (w) = $-1+x$, y, z; (x) = $1-x$, $2-y$, $2-z$; (y) = $-x$, $2-y$, $2-z$]; Right: $\pi\cdots\pi$ stacking interactions (red dotted lines) in **1**. The H atoms left and right, triazine ring of tptz, left, and one (left)/two (right) cyanido groups were removed for the sake of clarity.

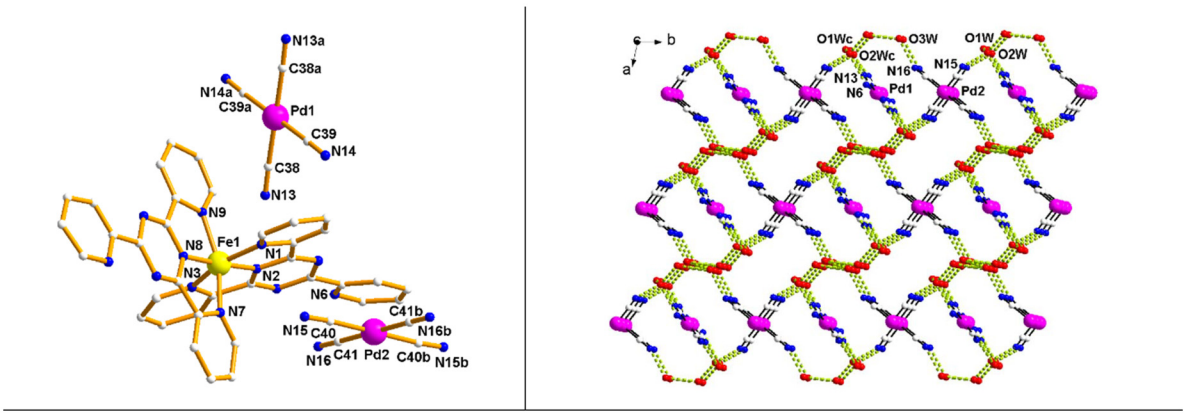

Fig. 3 Left: crystal structure of **3**, together with the atom labelling scheme. The solvent molecules are omitted for clarity; symmetry codes: (a) = $2-x$, $1-y$, $1-z$; (b) = $2-x$, $2-y$, $2-z$. Right: a view along a axis of the hydrogen bonding pattern in **3**. (c) = x, $-1+y$, z.

ligands, with the N6 donor atoms describing a distorted octahedral geometry within the $[Fe(tptz)_2]^{2+}$ complex ions [the estimated ChSM value is 2.423 for Fe1 in **3**, and 2.484 (**4**), and zero for the ideal octahedron as estimated by SHAPE program;[56,57] see Table S3 in the ESI†]. The two chelating tptz ligands enclose the Fe(II) cation in a rigid pocket and, therefore, the Fe–N_{tptz} bond lengths are shorter than those for compounds **1** and **2**, ranging between 1.862(5) and 2.014(5) Å for **3** and between 1.862(4) and 1.999(4) Å for **4** (see also Table S2 in the ESI†). These values suggest a low spin state for the Fe(II) ion, as opposed to Fe^{II}_{HS} in **1** and **2**. The Pd(II) ions from the two separated anionic units are surrounded by four cyanido ligands in a slightly distorted square planar geometry. The angles between adjacent CN^- ligands are close to a right angle, being 89.2(3) and 90.8(3)° for Pd1 (C38–Pd1–C39 and C38–Pd1–C39b) and ranging between 87.8(10) and 92.2(10)° for Pd2 (see also Table S2 in the ESI†). The Pd1–C bond lengths are 2.009(10) (Pd1–C38) and 2.013(9) Å (Pd1–C39), whereas, in the second $[Pd2(CN)_4]^-$ unit the Pd2–C distances range between 2.016(10) and 2.026(8) Å.

Hydrogen bonds are established between water solvent molecules and cyanido groups belonging to the $[Pd(CN)_4]^{2-}$ anions forming a 3-D supramolecular network, as shown in Fig. 3, right and Fig. S15, right (for **4**, see Fig. S14, right Tables S6 and S7 in the ESI†). The aromatic pyridine cycles are involved in offset and edge-to-face π···π stacking interactions, each $[Fe(tptz)_2]^{2+}$ fragment being connected to other five neighboring fragments (see Fig. S16 in the ESI†).

Magnetic properties

Variable temperature magnetic susceptibility measurements on compound **1**, illustrated as $\chi_M T$ *vs.* T plot [χ_M is the magnetic susceptibility per mole of compound], in Fig. 4 left, show a value of 3.62 $cm^3\ mol^{-1}$ K, at room temperature, as expected for a high-spin hexacoordinated Fe(II), since the Pd(II) ion is diamagnetic. Upon cooling, $\chi_M T$ decreases slowly down to *ca.* 3.3 $cm^3\ mol^{-1}$ K, at *ca.* 120 K. Below 120 K, the value of $\chi_M T$ decreases abruptly indicating the presence of an incomplete sharp HS-to-LS SCO with a $T_{1/2}$ value of *ca.* 105 K. Incomplete or partial spin transitions are not uncommon for the Hofmann type clathrates or other cyanido bimetallic networks.[31,59,60] At low temperatures, the $\chi_M T$ value decreases due to the zero-field-splitting (ZFS) effect on the HS Fe^{II} ions fraction. The variable-field magnetization measurements were not found to reach saturation between 2.0 and 5.0 K, shown in Fig. 4, right, which indicates the occurrence of magnetic anisotropy. Furthermore, the *M vs. H*/*T* curves do not superpose on one another, also implying a relatively important magnetic anisotropy of the high-spin iron(II) in **1** which represents the part of the iron complex that did not undergo the crossover transformation.

The magnetic properties of **2** are shown in the form of $\chi_M T$ *vs.* T and *M vs. H* plots, Fig. 5. At room temperature, the value of the $\chi_M T$ product is 3.8 $cm^3\ mol^{-1}$ K, as expected for a high-spin Fe(II) ion. Upon cooling, $\chi_M T$ decreases slowly down to *ca.* 3.2 $cm^3\ mol^{-1}$ K, at *ca.* 50 K indicating an incomplete gradual HS-to-LS SCO.

To estimate the contribution of the magnetic anisotropy in the magnetic susceptibility for compounds **1** and **2**, we modelled the magnetic properties using an anisotropic Hamiltonian containing the two components of the ZFS (axial (D) and rhombic (E)) (eqn (1)):[52,61]

$$\hat{H} = D\left(\vec{\hat{S}}_z^{\,2} - S(S+1)/3\right) + E\left(\vec{\hat{S}}_x^{\,2} - \vec{\hat{S}}_y^{\,2}\right) + \mu_B g \vec{\hat{S}} H \quad (1)$$

In order to consider the spin crossover phenomenon, the magnetic susceptibility has been analyzed by taking into account the convection factor "c" which represents the mole fraction of Fe(II) that undergoes the HS-to-LS SCO transformation (eqn (2)):

$$\chi T = c\{\chi T_{HS}\}_a + (1-c)\{\chi T_b\} \quad (2)$$

The crossover phenomenon itself was defined by classical thermodynamic parameters (eqn (3) and (4)):[52]

$$\{\chi T\}_b = x\{\chi T_{HS}\}_b + (1-x)\{\chi T_{LS}\}_b \quad (3)$$

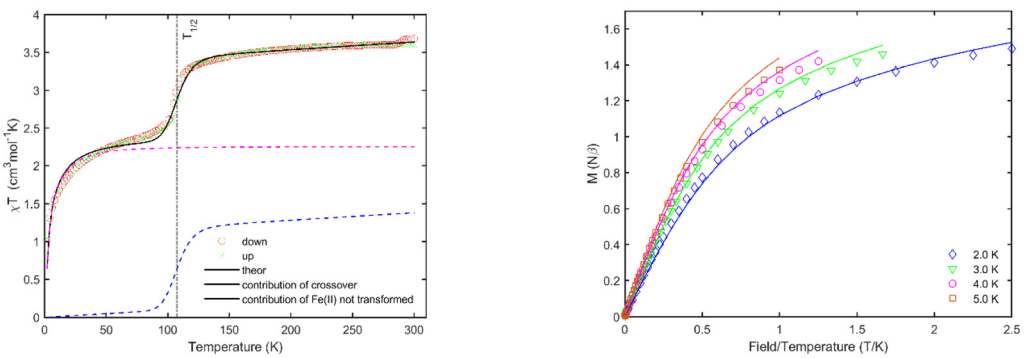

Fig. 4 Left: temperature dependence of magnetic susceptibility $\chi_M T$ as a function of temperature (T) for compound **1**. The solid line represents the theoretical value of magnetic susceptibility. The blue dashed lines represent the contributions of the crossover transformations. The pink dashed line represents the contribution of the non-transformed part of iron complexes. Right: Reduced magnetization plots for **1** at an indicated temperature. The solid lines correspond to the best fit (see the text).

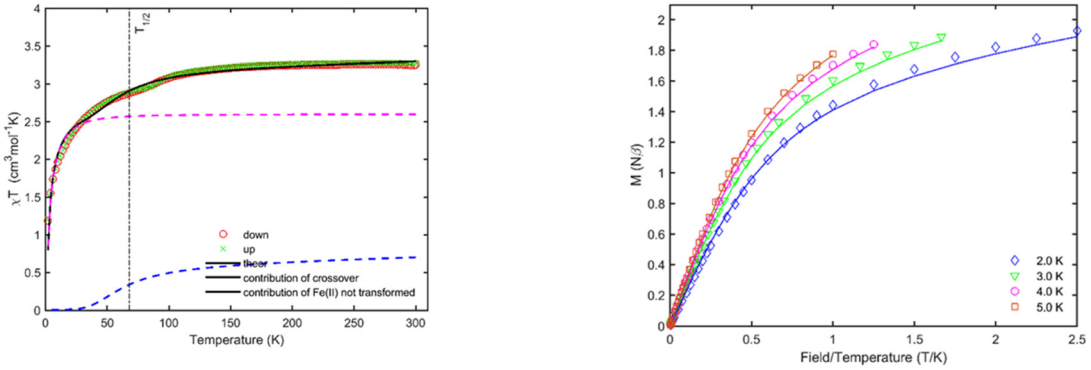

Fig. 5 Left: temperature dependence of magnetic susceptibility $\chi_M T$ as a function of temperature (T) for compound **2**. The solid line represents the theoretical value of magnetic susceptibility. The dashed lines represent the contributions of the crossover transformations. Right: reduced magnetization plots for **2** at indicated temperature the solid lines correspond to the best fit.

$$x = \frac{1}{1 + \exp\left[\left(\frac{\Delta H}{R}\right)\left(\frac{1}{T} - \frac{1}{T_c}\right)\right]} \quad (4)$$

The variation of the magnetic susceptibility with temperature, as well as the dependence of the magnetization function of the field strength, were analyzed together to constrain the multiple variable parameters. Additionally, we also considered the temperature-independent second-order Zeeman contribution of LS Fe(II) (t_{2g}^6), which was fixed with values of χ_{LS} = 0.003 cm^3 mol^{-1}.[62] Two types of adjustments were performed, one for $D < 0$ and one for $D > 0$, while imposing the condition $D > 3E$. The fits for $D > 0$ show a better coincidence between theoretical and experimental data.

This result is also consistent with the absence of the signal in the out-of-phase components of ac susceptibility (χ'') at zero dc field and when applying a small dc field (0.1, 0.2 T). The best agreement between experimental and theoretical data was obtained for the following values of the variable parameters: c = 0.67(3), ΔH = 15.7 kJ mol^{-1}, ΔS = 145 J mol^{-1} K^{-1}, T_c = 108(1) K, g = 2.11(2), D = 11.5(1) cm^{-1}, E = 3.8(7) cm^{-1} for compound **1**, and c = 0.81(6), ΔH = 1.7 kJ mol^{-1}, ΔS = 25 J mol^{-1} K^{-1}, T_c = 68 K, g = 2.07(2), D = 8.6(1) cm^{-1}, E = 2.9(5) cm^{-1} for compound **2**, respectively. The values obtained for the thermodynamic parameters correspond to the transition of one mole of the substance. To apply these parameters to the substance under study, they were multiplied by the factor $(1 - c)$, which represents the mole fraction of the complex undergoing SCO. The final values of the thermodynamic parameters are ΔH = 5.18 kJ mol^{-1} and ΔS = 47.85 J mol^{-1} for compound **1**, and ΔH = 0.3 kJ mol^{-1}; ΔS = 4.75 J mol^{-1} for compound **2**. The results are shown in Fig. 4 and 5, left which also shows the dependence of the magnetic susceptibility variation with temperature for the Fe(II)–HS parts involved (blue) and the part not involved (red) in the crossover transformation. The values of the magnetic anisotropy parameters (D, E), as well as the g-factor are in good agreement with those known in the literature.[61,63–66]

The Slichter–Drickamer model[52,67] can similarly be applied to estimate thermodynamic parameters by focusing solely on the upper part of the magnetic susceptibility data for compound **1**, where the transition is clearly represented. This model was employed in the simulation mode (Fig. S17 in the ESI†). The thermodynamic data obtained are ΔH = 5.3 kJ mol^{-1} ΔS = 48.62 J mol^{-1}. Additionally, this model enabled the estimation of the interaction parameter, which is approximately γ = 1.2 kJ mol^{-1}. Notably, the value obtained for γ is lower than $2RT_c$ = 1.8 kJ mol^{-1}, which corresponds to the absence of hysteresis in these compounds and is consistent with findings from other studies in the literature.[68,69]

The compounds **3** and **4** are diamagnetic in the temperature range of 2–400 K, as expected taking into account the values of the Fe–N distances which indicate a low spin state for Fe(II). It is worth mentioning that these compounds show a different magnetic behavior compared to the high-spin $[Fe^{II}(tptz)(NO_3)(MeOH)_2](NO_3)$ previously reported.[45]

Although the distortion degree of the Fe(II) geometry is low and the value is very close for both pairs of complexes, **1** and **2**, as well as for **3** and **4**, the magnetic properties differ significantly. This can be explained by the iron(II) coordination sphere which is not the same for compounds **1** and **2** against **3** and **4**. The Fe(II) ion in the structures of **3** and **4** is coordinated by two tptz tridentate ligands and this environment, most likely, determines a more compact (and rigid) arrangement and a smaller, low-spin metal ion, to accommodate the two large pincer ligands. For the chains (**1** and **2**), the coordination of the cyanido metalloligand to the $\{Fe^{II}tptz\}$ moiety, led to longer Fe–$N_{cyanide}$ distances, and there was also a significant increase in the Fe–N_{tptz} bond lengths. In **1** and **2**, the substitution of the second tptz ligand with much smaller cyanide ligands in the coordination sphere of Fe(II), is beneficial for the SCO behavior, since the Fe(II) metal ion has enough space and is a high spin, larger ion.

^{57}Fe Mössbauer spectroscopy

In contrast to the bulk magnetic susceptibility measurements, Mössbauer spectroscopy is a local method, directly probing

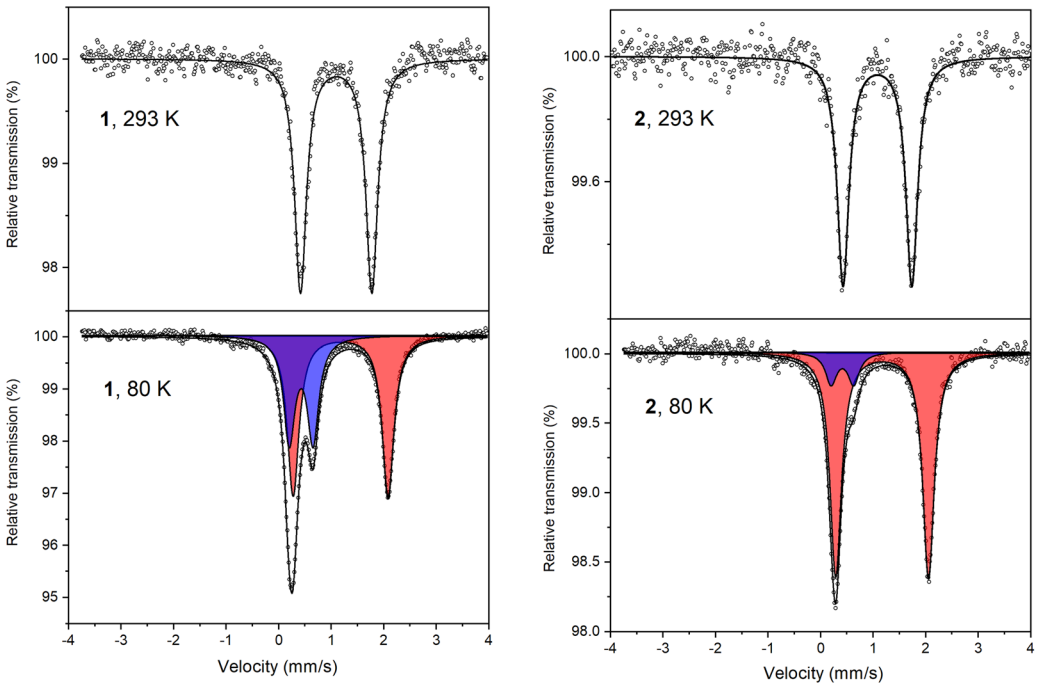

Fig. 6 Mössbauer spectra of **1** and **2** recorded at 80 and 293 K. At 80 K, the deconvoluted spectra of HS and LS Fe(II) are shown in red and blue, respectively.

Table 3 Hyperfine parameters obtained from the Mössbauer spectra of **1** and **2** at 80 and 293 K, and relative intensities of HS and LS quadrupole doublets

	1			**2**		
	δ (mm s^{-1})	ΔE_Q (mm s^{-1})	%	δ (mm s^{-1})	ΔE_Q (mm s^{-1})	%
293 K, HS	1.092(2)	1.357(3)	100	1.084(3)	1.308(5)	100
80 K, HS	1.177(2)	1.806(4)	61(3)	1.169(2)	1.765(4)	88(2)
80 K, LS	0.427(4)	0.440(8)	39(3)	0.415(7)	0.431(19)	12(2)

the state of all Fe atoms in the sample. In Fig. 6 are depicted the ^{57}Fe Mössbauer spectra for **1** and **2**. At 293 K, the spectra of **1** and **2** show a single quadrupole doublet with the isomer shift δ of 1.092(2) and 1.084(3) mm s^{-1} and quadrupole splitting ΔE_Q of 1.357(3) and 1.308(5) mm s^{-1} for **1** and **2**, respectively. The hyperfine parameters indicate the HS state of Fe(II) and are typical of $\{Fe^{II}M^{X}\}$ cyanidobimetallic complexes, where M is a diamagnetic metal ion (x = I and II).[25,32] At 80 K, the second doublet with δ = 0.427(4) and 0.415(7); ΔE_Q = 0.440(8) and 0.431(19) mm s^{-1} appears for **1** and **2**, respectively. The parameters are characteristic of LS Fe(II) in the distorted octahedral FeN_6 ligation.

At the same time, δ of the HS doublet exhibits a positive shift on cooling to 80 K due to the second-order Doppler shift. Increase of ΔE_Q at low temperature is also typical of HS Fe(II) in an axial electric field. The relative intensity of the LS doublet in **1** and **2** at 80 K is found to be 39(3)% and 12(2)%, which corresponds well to $\chi_M T$ = 2.3 and 3.3 cm^3 mol^{-1} K, respectively. The ^{57}Fe hyperfine parameters for **1** and **2** are summarized in Table 3.

Conclusions

We report on two new SCO iron(II) ladder-like 1-D coordination polymers using polydentate and chelating tptz ligands and cyanido-based $[M^{II}(CN)_4]^{2-}$ metalloligands (M = Pd, Pt) as assembling units. By employing the tptz pincer ligand, we provide an interesting alternative to design and construct iron (II) spin transition coordination polymers. Besides, these are the first examples of spin transition occurring in complexes including the $\{Fe^{II}(tptz)\}$ moiety. The importance of the coordination surrounding of iron(II) and cooperativity effect in triggering SCO properties is best illustrated by comparing the magnetic behavior of the two cyanido-bridged $\{Fe^{II}Pd^{II}\}$ and $\{Fe^{II}Pt^{II}\}$ double chains (**1** and **2**) with the more soluble by-products of the reaction that consist of separated $[Fe^{II}(tptz)_2]^{2+}$ cations and $[M(CN)_4]^{2-}$ (M = Pd and Pt) anions (**3** and **4**). Thus, the rigid $Fe^{II}N_6$ closed environment in **3** and **4** provided by two chelating tptz ligands preserved the low-spin state for iron(II) even above room temperature (2–400 K), the samples being diamagnetic. Conversely, for **1** and **2**, the coordination

of one tptz and three CN^- ligands determines a more flexible iron(II) surrounding that allows the stabilization of HS and, on cooling, an incomplete HS–LS spin transition. We envisage exploring and enriching this new family of iron(II) SCO active coordination polymers with other types of pincer ligands that could lead to new architectures and, therefore, better opportunities to achieve switchable molecular materials.

Author contributions

Diana Visinescu: investigation and writing. Maria-Gabriela Alexandru: methodology, conceptualization, resources, writing, and supervision. Ghenadie Novitchi: investigation, resources, and writing. Sergiu Shova: investigation and methodology. Sergii I. Shylin: investigation and writing. Delia-Laura Popescu: investigation and methodology.

Conflicts of interest

There are no conflicts to declare.

Acknowledgements

This work was supported by a grant from the Romanian Ministry of Education and Research, CNCS – UEFISCDI, project number PN-III-P1-1.1-TE-2019-0352, within PNCDI III, and the Swedish Foundation for Strategic Research.

References

1 M. A. Halcrow, *Coord. Chem. Rev.*, 2009, **253**, 2493.
2 J. Olguín and S. Brooker, *Coord. Chem. Rev.*, 2011, **255**, 203.
3 M. C. Muñoz and J. A. Real, *Coord. Chem. Rev.*, 2011, **255**, 2068.
4 G. A. Craig, O. Roubeau and G. Aromí, *Coord. Chem. Rev.*, 2014, **269**, 13.
5 R. W. Hogue, S. Singh and S. Brooker, *Chem. Soc. Rev.*, 2018, **47**, 7303.
6 Z.-P. Ni, J.-L. Liu, M. N. Hoque, W. Liu, J.-Y. Li, Y.-C. Chen and M.-L. Tong, *Coord. Chem. Rev.*, 2017, **335**, 28.
7 H. S. Scott, R. W. Staniland and P. E. Krüger, *Coord. Chem. Rev.*, 2018, **362**, 24.
8 R. W. Hogue, S. Singh and S. Brooker, *Chem. Soc. Rev.*, 2018, **47**, 7303.
9 M. Ruben, S. K. Kuppusamy, Y. Bayeh, T. G. Ashebr, F. Elemo, M. Gebrezgiabher and M. Thomas, *Dalton Trans.*, 2019, **48**, 15321.
10 O. I. Kucheriv, I. O. Fritsky and I. A. Gural'skiy, *Inorg. Chim. Acta*, 2021, **521**, 120303.
11 M. K. Javed, A. Sulaiman, M. Yamashita and Z.-Y. Li, *Coord. Chem. Rev.*, 2022, **467**, 214625.
12 B. Dey and V. Chandrasekhar, *Dalton Trans.*, 2022, **51**, 13995.
13 B. Weber, *Coord. Chem. Rev.*, 2009, **253**, 2432.
14 D. J. Rudd, C. R. Goldsmith, A. P. Cole, T. D. P. Stack, K. O. Hodgson and B. Hedman, *Inorg. Chem.*, 2005, **44**, 1221.
15 M. Boniolo, S. I. Shylin, P. Chernev, M. H. Cheah, P. A. Heizmann, P. Huang, N. Salhi, K. Hossain, A. Thapper, M. Lundberg and J. Messinger, *Chem. Commun.*, 2020, **56**, 2703.
16 V. A. Grillo, L. R. Gahan, G. R. Hanson, R. Stranger, T. W. Hambley, K. S. Murray, B. Moubaraki and J. D. Cashion, *J. Chem. Soc., Dalton Trans.*, 1998, 2341.
17 M. Yamasaki and T. Ishida, *Chem. Lett.*, 2015, **44**, 920.
18 J. Sánchez Costa, C. Balde, C. Carbonera, D. Denux, A. Wattiaux, C. Desplanches, J. P. Ader, P. Gütlich and J. F. Létard, *Inorg. Chem.*, 2007, **46**, 4114.
19 P. Guionneau, F. Le Gac, A. Kaiba, J. Sánchez Costa, D. Chasseau and J. F. Letard, *Chem. Commun.*, 2007, 3723.
20 J. J. Scepaniak, T. D. Harris, C. S. Vogel, J. Sutter, K. Meyer and J. M. Smith, *J. Am. Chem. Soc.*, 2011, **133**, 3824.
21 O. Kahn, *Curr. Opin. Solid State Mater. Sci.*, 1996, **1**, 547.
22 B. Weber, W. Bauer and J. Obel, *Angew. Chem.*, 2008, **120**, 10252; B. Weber, W. Bauer and J. Obel, *Angew. Chem., Int. Ed.*, 2008, **47**, 10098.
23 V. Martínez, A. Gaspar, M. C. Muñoz, G. Bukin, G. Levchenko and J. A. Real, *Chem. – Eur. J.*, 2009, **15**, 10960.
24 L. G. Lavrenova and O. G. Shakirova, *Eur. J. Inorg. Chem.*, 2013, 670.
25 S. I. Shylin, O. I. Kucheriv, S. Shova, V. Ksenofontov, W. Tremel and I. A. Gural'skiy, *Inorg. Chem.*, 2020, **59**, 6541.
26 K. Kitase and T. Kitazawa, *Dalton Trans.*, 2020, **49**, 12210.
27 K. Kitase, D. Akahoshi and T. Kitazawa, *Inorg. Chem.*, 2021, **60**, 4717.
28 V. M. Hiiuk, S. Shova, A. Rotaru, V. Ksenofontov, I. O. Fritsky and I. A. Gural'skiy, *Chem. Commun.*, 2019, **55**, 3359.
29 C. Bartual-Murgui, L. Salmon, A. Akou, N. A. Ortega-Villar, H. J. Shepherd, M. C. Muñoz, G. Molnár, J. A. Real and A. Bousseksou, *Chem. – Eur. J.*, 2012, **18**, 507.
30 N. F. Sciortino, K. R. Scherl-Gruenwald, G. Chastanet, G. J. Halder, K. W. Chapman, J.-F. Létard and C. J. Kepert, *Angew. Chem., Int. Ed.*, 2012, **51**, 10154.
31 K. A. Zenere, P. W. Doheny, S. G. Duyker, E. Trzop, E. Collet, B. Chan, C. J. Kepert and S. M. Neville, *Chem. Sci.*, 2018, **9**, 5623.
32 O. I. Kucheriv, S. I. Shylin, V. Ksenofontov, S. Dechert, M. Haukka, I. O. Fritsky and I. A. Gural'skiy, *Inorg. Chem.*, 2016, **55**, 4906.
33 V. M. Hiiuk, S. Shova, A. Rotaru, A. A. Golub, I. O. Fritsky and I. A. Gural'skiy, *Dalton Trans.*, 2020, **49**, 5302.
34 S. Kawabata, S. Chorazy, J. J. Zakrzewski, K. Imoto, T. Fujimoto, K. Nakabayashi, J. Stanek, B. Sieklucka and S.-I. Ohkoshi, *Inorg. Chem.*, 2019, **58**, 6052.
35 S. Chorazy, T. Charytanowicz, D. Pinkowicz, J. Wang, K. Nakabayashi, S. Klimke, F. Renz, S.-i. Ohkoshi and B. Sieklucka, *Angew. Chem.*, 2020, **132**, 15871.

36 S.-i. Ohkoshi, S. Takano, K. Imoto, M. Yoshikiyo, A. Namai and H. Tokoro, *Nat. Photonics*, 2014, **8**, 65.
37 A. Barakat, A. El-Faham, M. Haukka, A. M. Al-Majid and S. M. Soliman, *Appl. Organomet. Chem.*, 2021, e6317.
38 Z. Yue, H. Lu, Z. Li, S. Guo, J. Song, Y. Ren, Y.-Y. Huang, J. Lin and J.-Q. Wang, *CrystEngComm*, 2019, **21**, 5059.
39 S. A. Cotton, V. Franckevicius, M. F. Mahon, L. L. Ooi, P. R. Raithby and S. J. Teat, *Polyhedron*, 2006, **25**, 1057.
40 C. Lete, D. Visinescu, S. Shova, C. Maxim and M.-G. Alexandru, *J. Solid State Chem.*, 2022, **313**, 123292.
41 D. Visinescu, S. Shova, D.-L. Popescu and M.-G. Alexandru, *Crystals*, 2022, **12**, 1618.
42 M.-G. Alexandru, D. Visinescu, B. Braun-Cula, F. Lloret and M. Julve, *Eur. J. Inorg. Chem.*, 2018, 349.
43 J.-H. Wang, K. R. Vignesh, J. Zhao, Z.-Y. Li and K. R. Dunbar, *Inorg. Chem. Front.*, 2019, **6**, 493.
44 H. Zhao, N. Lopez, A. Prosvirin, H. T. Chifotides and K. R. Dunbar, *Dalton Trans.*, 2007, 878.
45 A. A. Hassoon, R. G. Harrison, N. Nawar, S. J. Smith and M. M. Mostafa, *J. Mol. Struct.*, 2020, **1203**, 127240.
46 C. P. Raptopoulou, Y. Sanakis and A. K. Boudalis, *Eur. J. Inorg. Chem.*, 2008, 5632.
47 *CrysAlisPro Software system*, Rigaku Corporation, Oxford, UK, 2015.
48 G. M. Sheldrick, *Acta Crystallogr., Sect. A: Found. Adv.*, 2015, **71**, 3.
49 G. M. Sheldrick, *Acta Crystallogr., Sect. C: Struct. Chem.*, 2015, **71**, 3.
50 O. V. Dolomanov, L. J. Bourhis, R. J. Gildea, J. A. K. Howard and H. Puschmann, *J. Appl. Crystallogr.*, 2009, **42**, 339.
51 H. Putz and K. Brandenburg, *Diamond—Crystal and Molecular Structure Visualization*, Crystal Impact, Bonn, Germany, 2014. Available online: **https://www.crystalimpact.com/diamond**.
52 O. Kahn, *Mol. Magn.*, 1993, 97.
53 P. Pascal, *Ann. Chim. Phys.*, 1910, **19**, 5.
54 S. Stoll and A. Schweiger, *J. Magn. Reson.*, 2006, **178**, 42.
55 S. De, L.-M. Chamoreau, H. El Said, Y. Li, A. Flambard, M.-L. Boillot, S. Tewary, G. Rajaraman and R. Lescouëzec, *Front. Chem.*, 2018, **6**, 326.
56 A. Mondal, Y. Li, L.-M. Chamoreau, M. Seuleiman, L. Rechignat, A. Bousseksou, M.-L. Boillot and R. Lescouëzec, *Chem. Commun.*, 2014, **50**, 2893.
57 M. Llunell, D. Casanova, J. Cirera, J. M. Bofill, P. Alemany, S. Alvarez, M. Pinsky and D. Avnir, *SHAPE: Continuous shape measures of polygonal and polyhedral molecular fragments, 1.1b*, University of Barcelona, Barcelona, 2005.
58 D. Casanova, M. Llunell, P. Alemany and S. Alvarez, *Chem. – Eur. J.*, 2005, **11**, 1479.
59 M. J. Murphy, K. A. Zenere, F. Ragon, P. D. Southon, C. J. Kepert and S. M. Neville, *J. Am. Chem. Soc.*, 2017, **139**, 1330.
60 E. Milin, V. Patinec, S. Triki, E.-E. Bendeif, S. Pillet, M. Marchivie, G. Chastanet and K. Boukheddaden, *Inorg. Chem.*, 2016, **55**, 11652.
61 R. Boča, *Theoretical Foundations of Molecular Magnetism*, 1999.
62 C. M. Harris and E. Sinn, *Inorg. Chim. Acta*, 1968, 296.
63 R. Boča, *Coord. Chem. Rev.*, 2004, **248**, 757.
64 Z. Yan, Z.-P. Ni, F.-S. Guo, J.-Y. Li, Y.-C. Chen, J.-L. Liu, W.-Q. Lin, D. Aravena, E. Ruiz and M.-L. Tong, *Inorg. Chem.*, 2014, **53**, 201.
65 M. Zając, I. E. Lipiński and C. Rudowicz, *J. Magn. Magn. Mater.*, 2016, **401**, 1068.
66 G. Novitchi, S. Jiang, S. Shova, F. Rida, I. Hlavička, M. Orlita, W. Wernsdorfer, R. Hamze, C. Martins, N. Suaud, N. Guihéry, A.-L. Barra and C. Train, *Inorg. Chem.*, 2017, **56**, 14809.
67 C. P. Slichter and H. G. Drickamer, *J. Chem. Phys.*, 1972, **56**, 2142.
68 C. J. Adams, M. C. Muñoz, R. E. Waddington and J. A. Real, *Inorg. Chem.*, 2011, **50**, 10633.
69 T. Cao, F. J. Valverde-Muñoz, X. Duan, M. Zhang, P. Wang, L. Xing, F. Sun, Z. Zhou, H. Liu, J. Jiang, M. C. Muñoz, J. A. Real and D. Zhang, *Inorg. Chem.*, 2021, **60**, 11048.